

Thermophysical Behavior of Armature Materials During a Pulsed Electrical Discharge

Subcontractor Report
prepared by

A. E. Zielinski, S. Niles, and J. D. Powell
U.S. Army Research Laboratory

19990504 138

April 1999

IAT.R 0192

Approved for public release; distribution unlimited.

The views, opinions, and/or findings contained in this report are those of the author(s) and should not be construed as an official Department of the Army position, policy, or decision, unless so designated by other documentation.

REPORT DOCUMENTATION PAGE

Form Approved
OMB NO. 0704-0188

Public reporting burden for this collection of information is estimated to average 1 hour per response, including the time for reviewing instructions, searching existing data sources, gathering and maintaining the data needed, and completing and reviewing the collection of information. Send comments regarding this burden estimate or any other aspect of this collection of information, including suggestions for reducing this burden, to Washington Headquarters Services, Directorate for Information Operations and Reports, 1215 Jefferson Davis Highway, Suite 1204, Arlington, VA 22202-4302, and to the Office of Management and Budget, Paperwork Reduction Project (0704-0188), Washington, DC 20503.

1. AGENCY USE ONLY (Leave blank)	2. REPORT DATE April 1999	3. REPORT TYPE AND DATES COVERED technical report 1/96-1/99	
4. TITLE AND SUBTITLE Thermophysical Behavior of Armature Materials During a Pulsed Electrical Discharge		5. FUNDING NUMBERS Contract # DAAA21-93-C-0101	
6. AUTHOR(S) A. E. Zielinski, S. Niles, and J. D. Powell			
7. PERFORMING ORGANIZATION NAME(S) AND ADDRESS(ES) Institute for Advanced Technology The University of Texas at Austin 4030-2 W. Braker Lane, #200 Austin, TX 78759		8. PERFORMING ORGANIZATION REPORT NUMBER IAT.R 0192	
9. SPONSORING / MONITORING AGENCY NAME(S) AND ADDRESS(ES) U.S. Army Research Laboratory ATTN: AMSRL-WM-B Aberdeen Proving Ground, MD 21005-5066		10. SPONSORING / MONITORING AGENCY REPORT NUMBER	
11. SUPPLEMENTARY NOTES The view, opinions and/or findings contained in this report are those of the author(s) and should not be considered as an official Department of the Army position, policy, or decision, unless so designated by other documentation.			
12a. DISTRIBUTION / AVAILABILITY STATEMENT Approved for public release; distribution unlimited.		12b. DISTRIBUTION CODE A	
13. ABSTRACT (Maximum 200 words) A technique is developed to measure the surface temperature of an electrical conductor during a pulsed electrical discharge. The technique of two-color interferometry (radiometry) is used to make the temperature measurements. This report explains the technique and the issues encountered in performing such measurements. Also, a theoretical model for the current and heat transport for the pulsed conductor is developed. Predicted and experimental results are compared. The measurements can yield isothermal data that can be used to corroborate calculated current distributions in solid armature railgun operation.			
14. SUBJECT TERMS action integral, thermophysical properties, infrared, radiometry, current distribution		15. NUMBER OF PAGES 36	
		16. PRICE CODE	
17. SECURITY CLASSIFICATION OF REPORT Unclassified	18. SECURITY CLASSIFICATION OF THIS PAGE Unclassified	19. SECURITY CLASSIFICATION OF ABSTRACT Unclassified	20. LIMITATION OF ABSTRACT UL

Table of Contents

1. Introduction.....	2
2. Design and Set-up of the Temperature Measurement Technique.....	4
A) Temperature Measurement Technique	4
B) Equipment.....	6
i) Detectors and Amplifiers.....	6
ii) Fiber Optic Cable	6
iii) Infrared Filters.....	6
iv) System.....	7
C) Temperature Measurement Calibration	8
D) Pulsed Measurements	11
E) Data Analysis.....	14
i) Numerical Technique.....	14
ii) Steady-State Evaluation of Thermophysical Properties.....	15
3. Theoretical Assessment	19
4. Calculations and Comparison with Experiment.....	21
5. Implementation in a Moving Armature.....	26
6. Summary and Conclusions.....	28
7. Acknowledgement	29
8. References	30
9. Appendix.....	31
10. Distribution List.....	35

List of Figures

Figure 1. Schematic Illustration of Rod Sample Test Fixture.....	3
Figure 2. Calculated Radiant Intensity for 200 °C and 700 °C Thermal Sources	5
Figure 3. Photograph of the Calibration Set-up	9
Figure 4. Typical Detector Outputs as a Function of Time (Source Temperature = 280 °C)	9
Figure 5. Infrared Measurement Technique Calibration.....	10
Figure 6. Photograph of the Pulsed-Measurement Set-up	11
Figure 7. Typical Measured Rod Voltage and di/dt Data as a Function of Time	13
Figure 8. Typical Rod Current and Dissipated Energy as a Function of Time	13
Figure 9. Peak Magnetic Field as a Function of Radial Distance from the Rod Sample	14
Figure 10. Typical Detector Outputs as a Function of Time for a Pulsed Current	15
Figure 11. Measured Surface Temperature as a Function of Time ($V_i = 1.1 \text{ kV}$).....	16
Figure 12. Specific Heat as a Function of Temperature	17
Figure 13. Resistivity as a Function of Temperature.....	18
Figure 14. Specific Action as a Function of Temperature	19
Figure 15. Measured and Predicted Surface Temperature ($V_i = 1.4 \text{ kV}$).....	24
Figure 16. Resistive Voltage Contribution Across the Rod Sample.....	25

List of Tables

Table 1. Summary of Fitting Constants for Surface Temperature as a Function of Time	16
Table 2. Summary of Surface Temperatures and Pulsed Power Data.....	21

Thermophysical Behavior of Armature Materials During a Pulsed Electrical Discharge

Alexander E. Zielinski, Steven Niles, and John D. Powell

Preface

A technique is developed to measure the surface temperature of an electrical conductor during a pulsed electrical discharge. The technique of two-color interferometry (radiometry) is used to make the temperature measurements. The infrared energies emitted from the conductor within two narrow bands are measured. The ratio of these energies can be compared to the ratios given from the energy distribution of a calibrated thermal source through these same bands. A continuum of temperatures can be sampled from the source to correlate the source temperature with the emitted infrared energies. The ratio of the energies can be used to determine the temperature of the conductor. Values for the resistivity and specific heat are determined up to 470 °C.

This report explains the technique and the issues encountered in performing such measurements. Also, a theoretical model for the current and heat transport for the pulsed conductor is developed. Predicted and experimental results are compared. The measured thermal data support the assumption of a slightly nonuniform distribution in the current. This non-uniformity is suspected of causing the rod to fail prematurely. This technique can be adapted to measure the temperature distribution of a solid armature, on a time scale shorter than that of the thermal propagation. The measurements can yield isothermal data that can be used to corroborate calculated current distributions in solid armature railgun operation.

1. INTRODUCTION

An electromagnetic railgun converts stored electrical energy into kinetic energy via magnetic forces. The magnetic force is created from an armature that carries current from rail to rail in two parallel conductors contained in the gun structure. There are many types of armatures that can be used in the railgun. Typical materials used in the fabrication of armatures are copper and aluminum. The overall effectiveness of a railgun is highly dependent upon the characteristics of the armature. Moreover, the efficacy of the armature is highly dependent upon its current distribution and, consequently, the thermal and mechanical loads imposed on the armature conductor. Theoretical models have been developed to calculate the current and heat diffusion in the solid armature [1, 2]. However, there are few data to support or discredit these models. The current distribution cannot be measured directly. However, optical techniques are non-intrusive, will not perturb the magnetic field or conductor geometry, and offer an indirect method to study the effects of field diffusion on a time-scale appropriate for electromagnetic launchers. The purpose of developing the temperature measurement technique is to infer the current diffusion process during application of a pulsed current by examining the thermal distribution on the surface of the conductor.

Time scales of interest for the railgun are on the order of a few milliseconds. The environment surrounding the railgun structure can be rich in electric and magnetic fields. Prior measurements utilized thermocouples to record the thermal load in a railgun bore during a pulsed current [3, 4]. However, the response times achieved in these experiments are, at best, *10 ms*. Significant experimental errors can produce unreliable data and yield very little corroboration to the theory. In order to benchmark the two-color measurement technique, it is desirable to perform the thermal measurements on a well-defined, axisymmetric conductor geometry. A *6.3-mm* diameter rod sample was chosen because it was well suited to use with available pulsed power, hardware, and predicted thermal loads. Aluminum and copper rods, with length-to-diameter ratio greater than *10*, were used for the conductor sample. A coaxial topology was selected for the fixture that delivers the current to the rod. The rod sample was attached in the center of the fixture. This location minimizes lateral forces on the rod. A tube exterior to the rod sample conducted the return current. The tube had holes machined through the diameter to allow

for viewing the rod sample (i.e., viewport) and attachment of other electrical instrumentation. Use of a coaxial fixture also minimized the external magnetic field generated by the high current flowing through the rod sample. A schematic illustration of the fixture is shown in Figure 1.

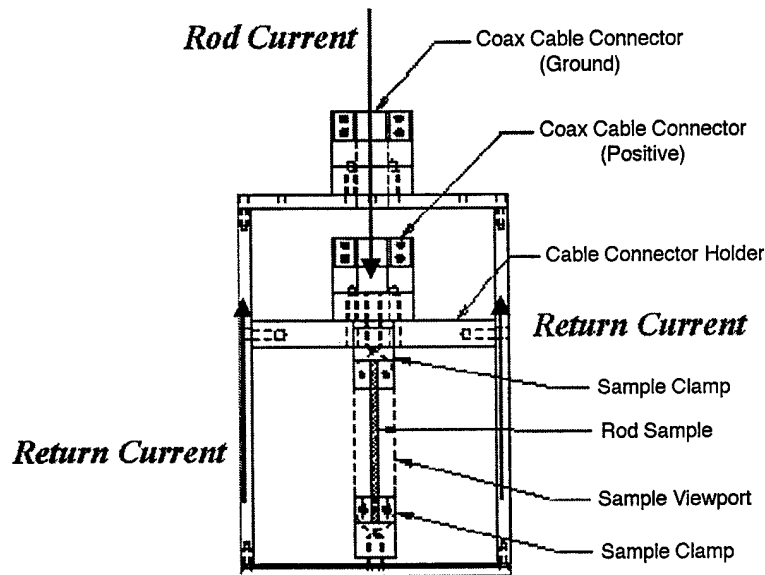


Figure 1. Schematic Illustration of Rod Sample Test Fixture.

A 1.6-MJ capacitor-based, pulsed power supply (PPS) was used to deliver energy to the rod samples. The capacitor bank is located at the Transonic Experimental Facility, Aberdeen Proving Ground, MD. The PPS is comprised of eight modules, each nominally 200 kJ at a maximum charge voltage of 10 kV. With the fixture, rod sample, and coax cable as the electrical load, the PPS will produce a nominal admittance of 90 kA/kV.

In addition to the infrared thermal measurements, the voltage across the rod (V_r), the time rate of change in the rod current (di/dt), and the time rate of change in the azimuthal component of the magnetic induction of the rod (dB_θ/dt) were measured. These data then complete the thermophysical characterization of the conducting rod sample.

A time-dependent formulation for the current and heat transport in the rod sample was developed. The model is one-dimensional (1-D) and accounts for the temperature-dependent material properties up to the melt temperature. Results from the calculations include the magnetic induction as well as the current distribution and temperature as a function of both space and time. The surface temperatures are compared to the experimentally measured values.

The report is organized as follows. In Section 2 the measurement technique is explained. Calibration and pulse-test data are analyzed. In Section 3 the one-dimensional model for the current and heat transport is described. In Section 4 the calculations are compared with the experimental results. The next section describes the implementation of the technique in a moving armature. In the last section, the summary and conclusions are presented.

2. DESIGN AND SET UP OF THE TEMPERATURE MEASUREMENT TECHNIQUE

A) Temperature Measurement Technique

The theory of using the two-color temperature measurement involves comparing the output of two infrared detectors. It has long been established that as the temperature of a source changes, the wavelength of its peak energy emission changes along with its emission amplitude [5]. Energy emission from a completely light-absorptive cavity is referred to as black body source. The radiant intensity of emission (E_r) as a function of wavelength λ can be written as

$$E_r(\lambda) = \frac{2\pi hc^2}{\lambda^5 [\exp(\frac{hc}{k\lambda T}) - 1]} \quad (1)$$

where h is Planck's constant ($6.62 \cdot 10^{-34}$ J-s), k is Boltzmann's constant ($1.38 \cdot 10^{-23}$ J/K), c is the speed of light ($2.99 \cdot 10^8$ m/s) and T is the temperature in Kelvin.

This same energy distribution can be applied to other objects by experimentally determining the emissivity and scaling the above equation accordingly. A plot of the preceding equation for source temperatures of 200 °C and 700 °C is shown in Figure 2. Equation 1 allows the infrared emission amplitudes to be related to the temperature of the source. For example, a black body source at 200 °C has a peak emissive wavelength of 6.12 μm and has a radiant intensity of $3.05 \cdot 10^8$. The 700 °C thermal source has peak emission at 2.98 μm with a radiant intensity of $1.12 \cdot 10^{10}$. If these emissions are passed through narrow band filters, the energy received through each filter for a given temperature will be unique over a selected temperature range. The filtered infrared energy at a specific temperature may be determined by multiplying the response of the filter by the energy radiated at a given wavelength. This procedure can be repeated for many source temperatures to give a profile of the expected output of the detectors over the anticipated temperature range. If the center frequencies and the bandwidth of the two filters are selected properly, the output from the detectors will be distinct. The ratio of these outputs can be calculated and plotted as a function of the source temperature. This correlation allows the determination of an unknown source temperature.

A theoretical model was developed to compute the ratios of the detector outputs given the center wavelengths of the filters and their respective half-maximum bandwidth. A listing of the code appears in the Appendix. This same numerical technique can be used for the dynamic armature measurement with a modification to model a fiber optic cable and any additional optics.

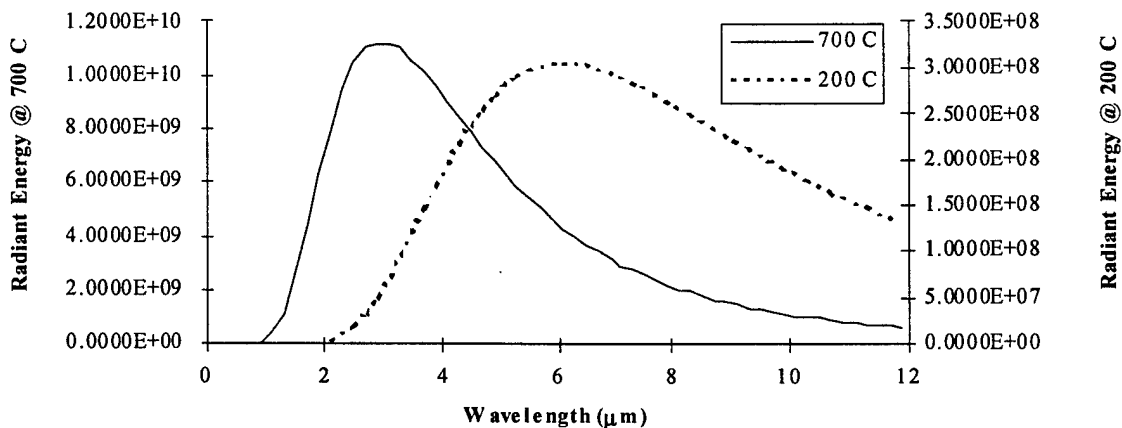


Figure 2. Calculated Radiant Intensity for 200 °C and 700 °C Thermal Sources.

B) Equipment

Ideal conditions and equipment are not always realized within practical time or budget constraints. This section addresses issues associated with implementing the infrared measurement technique in the laboratory environment.

i) Detectors and Amplifiers

The detectors used in this investigation were indium-antimonide (EG&G Judson model J-10D) and were cooled with liquid nitrogen. Each detector had a response of roughly 40% of peak at $2.6\ \mu m$, reaching a peak at approximately $4.6\ \mu m$ and then a steep roll-off for wavelengths greater than $5.3\ \mu m$. Electronic circuitry to amplify the output of the detector was readily available. One of the amplifiers had a 10^5 gain and the other a 10^6 gain. The higher gain amplifier was used in conjunction with the shorter wavelength filter because the emissions at the low end of the temperature range are very small. However, significantly more noise was introduced into the measurement for very low temperature emissions.

ii) Fiber Optic Cable

A fiber optic cable was to be used to transmit the infrared emissions to the detectors. Unfortunately, this cable suffered damage during a test in which the rod sample failed thermally and arced. However, during the measurements that were completed with the fiber optic cable several issues surfaced. With a plastic-clad, fluoride-glass fiber optic cable, significant attenuation of long wavelengths made it difficult to receive emissions greater than $4\ \mu m$. Also, emission loss due to the high numerical aperture of the cable was significant. With the fiber optic cable placed as close as possible to the detector surface, the divergence of the beam created a 1-mm diameter circle and the detector used a few percent of the transmitted energy.

iii) Infrared Filters

Based on theoretical predictions, values for the filters that produced distinguishable and distinct detector amplitude ratios were $2.99\ \mu m$ and $5.20\ \mu m$, each with a bandwidth of $0.10\ \mu m$. However, because of the characteristics of the entire measurement system, the $5.2\ \mu m$ filter was

replaced with a $3.975\ \mu\text{m}$ filter. Though not theoretically ideal, when used in conjunction with the other components of the system, this filter produced significantly better low temperature resolution.

iv) System

In the earlier measurements previously described, a detector was mated to a fiber optic cable by machined aluminum caps. These caps were slipped over the detector window and held on by a setscrew. The metal cap accommodated both the furl termination on the fiber optic cable as well as a 25-mm diameter filter. This arrangement worked well mechanically, but the room temperature emissions for the metal cap, filter and sleeve biased the detector. Fortunately, the bias was sufficiently small such that there was ample dynamic range to perform the measurements.

For the measurements described in this report a fiber optic cable was not used. The detectors were in direct view of the emissions from the thermal source (i.e., rod sample). The detectors were placed adjacent to one another and positioned symmetrically about the mid-length of the rod sample. Also, the detectors were placed as close as possible to the rod sample to reduce the optical losses, and yet far enough away to reduce the electric and magnetic field coupling from the experiment. Based on measurements of the magnetic field surrounding the fixture, it was determined that a distance greater than $0.18\ \text{m}$ was acceptable for the location of the detectors.

Other considerations accounted for minimizing the coupling of the electric and magnetic fields of the experiment with the detectors. To minimize noise, the detectors and amplifiers were powered directly from a regulated 12-V battery source. A digital oscilloscope that was not connected to the ac power ground monitored the output signals. A gasoline-powered generator supplied power to the data acquisition equipment and provided electrical isolation from the experiment. However, without shielding the detectors and their amplifiers, there is still a possibility of capacitively coupling the system or generating noise through the time rate of change in the electric field (dE/dt). Evidence of this coupling is seen in the detector output signals at the initiation of the discharge where dE/dt is the largest.

C) Temperature Measurement Calibration

Shown in Figure 3 is a photograph of the equipment used in the calibration of the detector output. The detectors were each matched to an amplifier for maximum frequency response. Each detector had the infrared filter located at the detector window and held in place with the machined aluminum caps. The $2.99\ \mu\text{m}$ filter and detector used the 10^6 gain amplifier while the $3.975\ \mu\text{m}$ filter and detector used the 10^5 gain amplifier. Both detectors were located $0.3\ \text{m}$ from a temperature controlled steel heat disk. The heat disk was painted with a high-temperature flat black paint (Krylon DH 1602, High-heat black). The rod samples were also painted so as to eliminate any variance in the measurements resulting from differences in emissivity. The oscilloscope was ac coupled to the detector amplifiers to remove the dc component from the signal. The thermal signal to the detector must change in order for an output to be present. In a pulsed discharge the temperature change at the surface occurs naturally. However, for the calibration tests, use of a known constant thermal source requires that the change in emission be provided externally. A light beam chopper wheel (Stanford Research Systems Model SR540) was used to block the emission from the heat disc and was located $0.298\ \text{m}$ away from the thermal source. The chopper wheel was located just in front of the detectors so as to minimize the heat conducted to the chopper wheel. The temperature of the heat source was monitored with a digital thermometer (Fluke model 52) and controlled by momentarily interrupting the power to the disk. Once the heat disk reached a steady state temperature, as indicated by the digital thermometer, the output voltage of the detector and amplifier pairs was recorded on a digital oscilloscope (Nicolet model 310).

A sample of the detector output for a source temperature of $280\ ^\circ\text{C}$ is plotted in Figure 4. The output voltage from each detector and amplifier pair was taken to be the average value when the chopper wheel was not obstructing the thermal source and corresponded to the time interval of $1\text{--}2\ \text{ms}$ for the $2.99\ \mu\text{m}$ filter and $2.5\text{--}3.5\ \text{ms}$ for the $3.975\ \mu\text{m}$ filter.

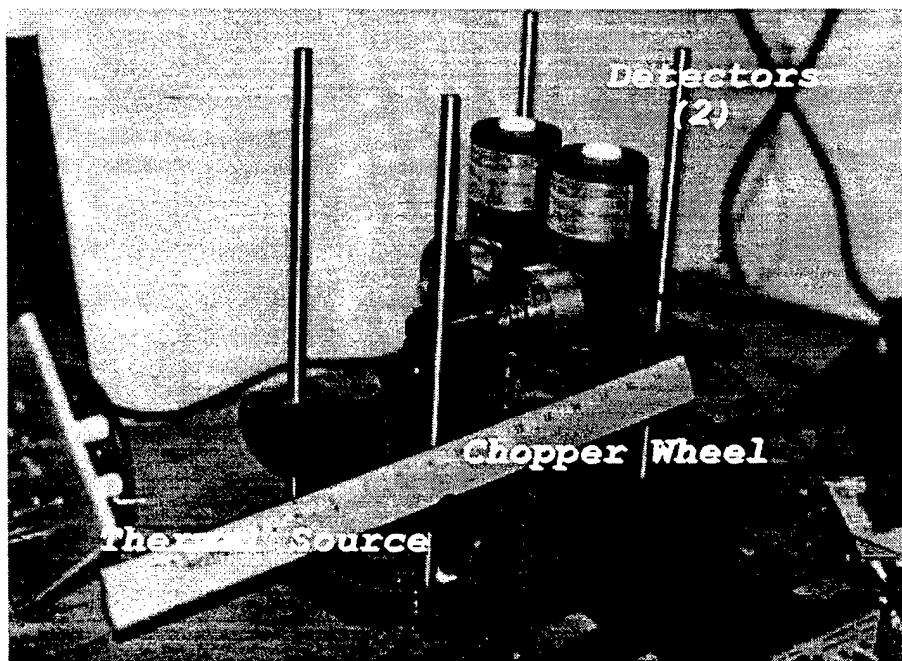


Figure 3. Photograph of the Calibration Setup.

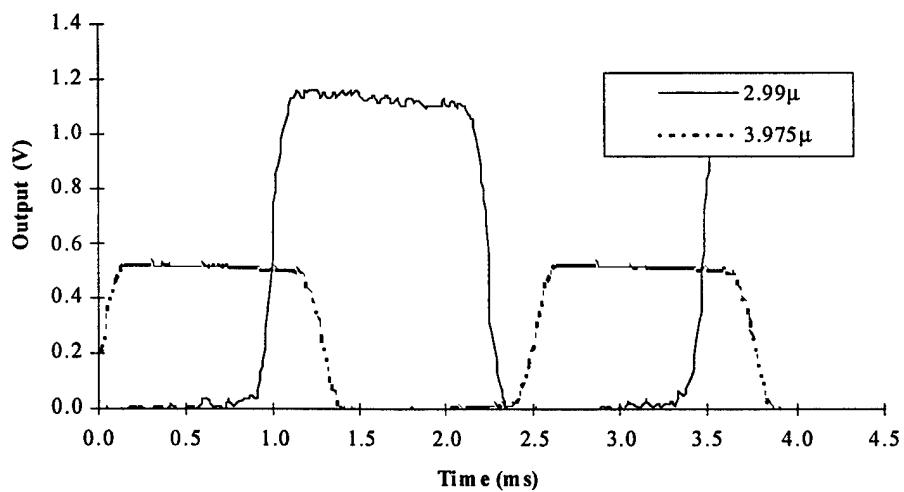


Figure 4. Typical Detector Outputs as a Function of Time (Source Temperature = 280 °C).

The ratio of the detector outputs for this source temperature is 2.2. The variability of the detector output voltage is less than 2% at this source temperature. However, the variability of the detector output voltage is greater than 10% for source temperatures less than 175 °C. The calibration procedure was repeated for source temperatures in the range of 125-500 °C and in increments of roughly 25 °C. A plot of the calibration data for each amplifier and detector pair is shown in Figure 5. Also shown in the figure is the calibration curve from the theory [see Equation (1) and Appendix]. In subsequent analysis, it was found to be convenient to convert the ratio of detector outputs to a temperature by using a functional fit to the calibration data. A power law was assumed and the fit is also shown in Figure 5. The equation that relates the source temperature (T_s) to the ratio of the detector output voltages (R) is

$$T_s = (227.2R)^{0.91}. \quad (2)$$

In addition to the magnitude of the detector output voltages, the time response of the detector and amplifier pair was also assessed. The velocity of the chopper wheel was measured from the chopper wheel controller as 133.3 rpm. The width of the detector-sensing window was 1 mm. The opening in the chopper wheel took 41 μ s to traverse from fully opened to fully obscured. The output signal rose to peak voltage in roughly 141 μ s. Therefore, the rise time of the detector and amplifier pair was calculated to be 100 μ s or 10 kHz. This response is favorable for observing the thermal response during pulsed events lasting a few milliseconds.

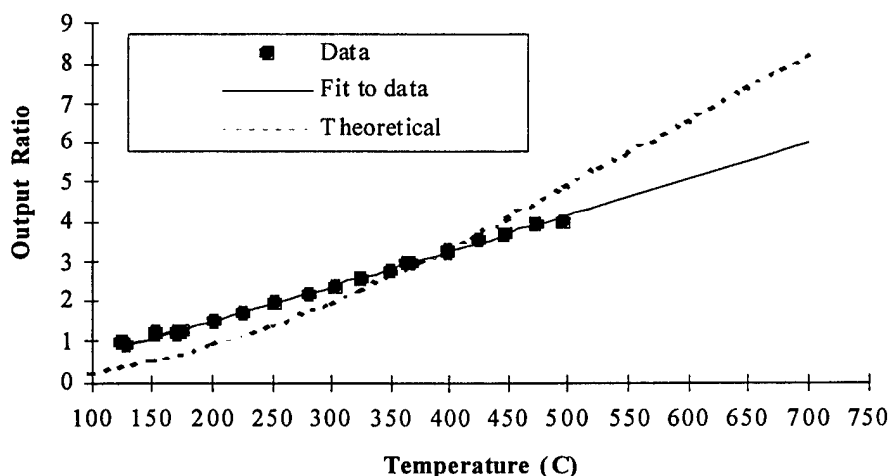


Figure 5. Infrared Measurement Technique Calibration.

D) Pulsed Measurements

The fixture (see Figure 1) was connected to the output of the PPS using a high-power coaxial cable [6]. The rod sample was mounted inside the fixture and was accessible through the sample viewport. The current from the PPS was conducted through the center of the fixture, through the rod sample, and returned to the PPS on the exterior of the fixture. The di/dt of the rod sample was measured at the output of the power supply. The voltage (V_r) was measured across the rod sample using an isolated technique. A nominal $100\text{-}\Omega$ resistor was placed across the rod sample. A current transformer (Pearson model 110a) was used to measure the current through the $100\text{-}\Omega$ resistor. The current transformer and resistor combination were calibrated as a function of frequency and found to have a nearly flat calibration constant of $1224:1$ to a frequency of 500 kHz .

As in the calibration tests, the detectors were placed 0.3 m from the rod sample. A small diameter tungsten wire was electrically heated inside the fixture near the location of the rod sample and was used to align the detectors with the rod sample surface prior to pulse testing. The position of the detectors was adjusted until maximum output signal voltage was found. The rod sample was secured to the fixture connections and was not removed after each pulse test. A photograph of the test set-up used for the transient measurements is shown in Figure 6.

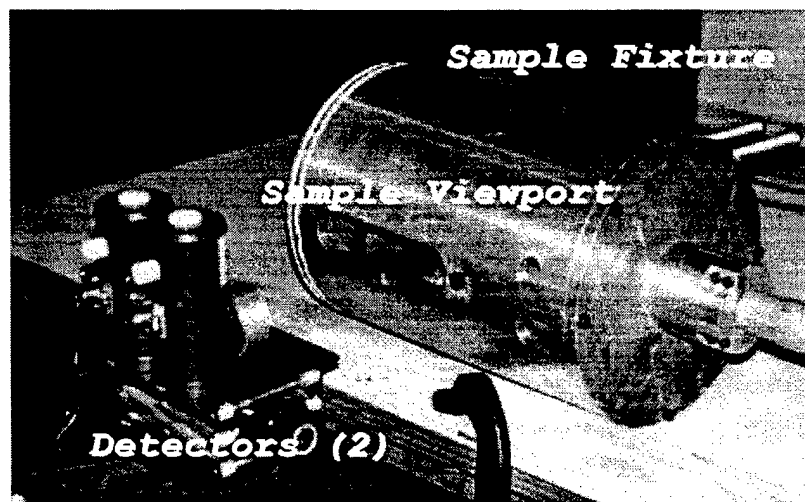


Figure 6. Photograph of the Pulsed-Measurement Setup.

Six tests were performed on the 6061-T6 aluminum rod sample and four tests were performed on the electrolytic tough pitch copper rod sample. Extreme care was taken when pulsing the rod samples near the current limit of the high-power coax and/or the melt temperature of the rod sample. Arcing during previous testing had caused detector, amplifier, and fiber optic cable failure.

Typical measured electrical data are plotted in Figure 7. As discussed, the voltage was measured across the rod sample using an isolated technique and the di/dt was measured at the output of the PPS. The rod sample for this test was aluminum and the initial capacitor voltage (V_i) was 1.1 kV . Shown in Figure 8 are the current, i , and energy, E , dissipated in the rod sample. The current as a function of time was obtained by numerically integrating the di/dt waveform. The energy was found by integrating the product of the current and the voltage measured across the rod sample. The current rose to a peak value of 100 kA at $420\text{ }\mu\text{s}$. Thereafter, the current decayed exponentially with a time constant of 1.8 ms . Both the current and voltage were small at 3 ms and maximum energy had been dissipated in the rod sample by 5 ms .

The dB/dt measurements were made using air-core coils wound with 10 turns of 24 -gauge wire on a 6.35 mm diameter form. The probes were calibrated in a transverse electromagnetic wave cell. Integration of the recorded signal output yields the magnetic induction (B_θ) in Tesla. Measurements were made of B_θ as a function of radial location on the mid-plane through the sample viewport. As expected, the magnetic induction waveform resembles the rod current waveform, and the peak magnetic induction (B_{pk}) was found to be proportional to the peak rod current. Additionally, the magnetic induction was found to be proportional to the inverse of the distance to the rod. The data, shown in Figure 9, are fit and scaled to 100 kA . Also indicated in the figure is the rod sample radius. On average, B_{pk} were found to be a few percent smaller on the sample viewport side of the rod than on the opposite side. The difference results from the removal of conducting material from the tube that forms the sample viewport.

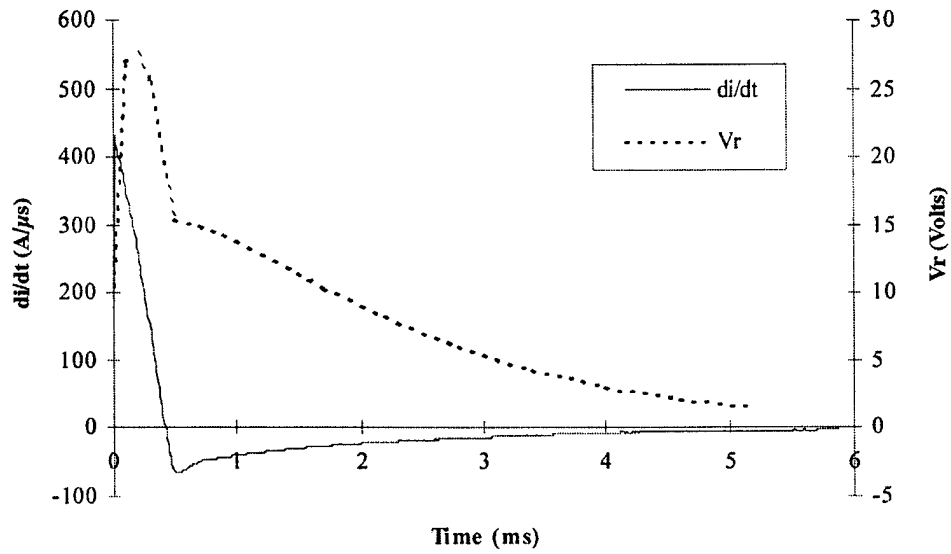


Figure 7. Typical Measured Rod Voltage and di/dt Data as a Function of Time.

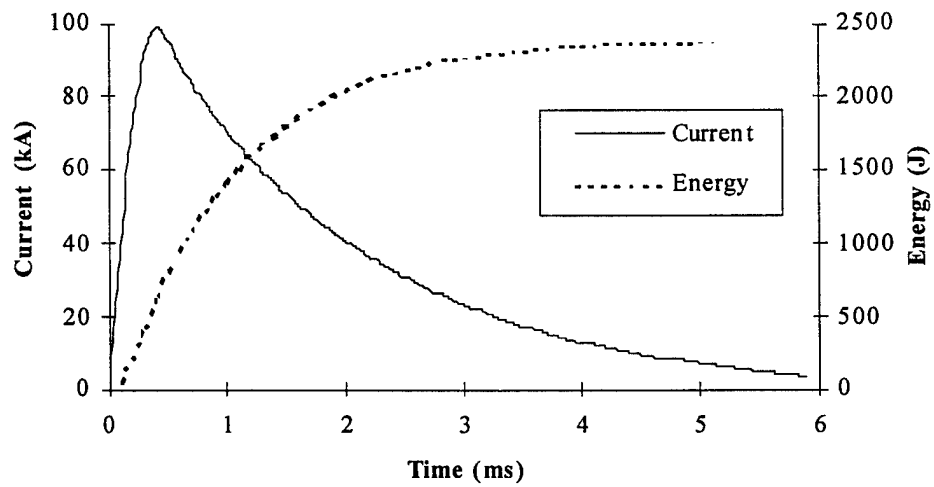


Figure 8. Typical Rod Current and Dissipated Energy as a Function of Time.

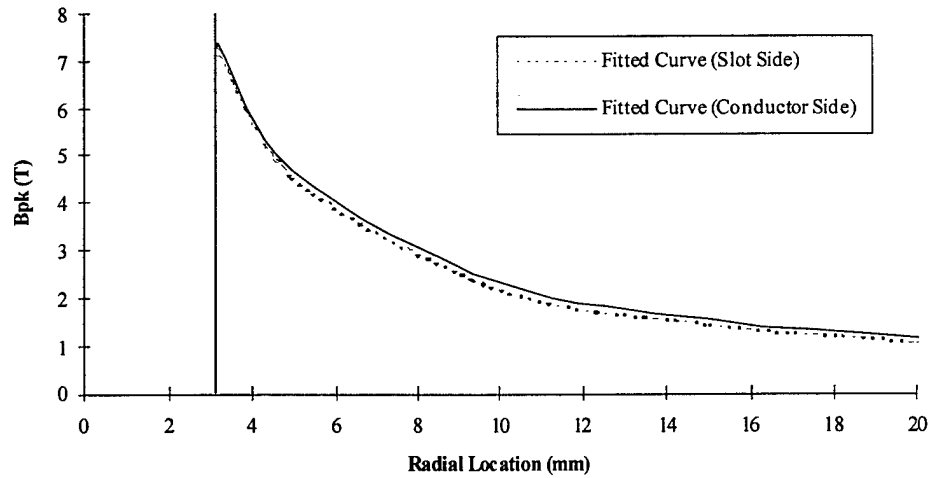


Figure 9. Peak Magnetic Field as a Function of Radial Distance from the Rod Sample.

The accuracy of the measurement of the magnetic induction, including probe calibration, and numerical integration, was estimated at 10%. Therefore, differences of less than 10% in B_θ cannot be determined. For a peak current of 100 kA the peak magnetic induction at the rod surface was extrapolated to be $7.1, \pm 0.07 \text{ T}$.

E) Data Analysis

i) Numerical Technique

The detector output voltages were recorded on a Nicolet digital oscilloscope at a rate of 0.5 MHz (2 $\mu\text{s}/\text{pt}$). The data were then transferred to a computer using VuPoint software [7]. Because the capacitively coupled detectors are susceptible to noise from the electromagnetic environment, large anomalous signal fluctuations were present for about 1 ms when the discharge was initiated. The baseline was established for the signals by taking the average of the data prior to initiation of the discharge. The outputs of the detectors are plotted in Figure 10. A fast Fourier transform of the data shows significant spectral content for frequencies less than 1 kHz. Therefore, the data were digitally filtered with a low pass filter having a cut-off frequency of 1 kHz.

As in the calibration tests, R was taken to be the ratio of the detector outputs and was calculated as a function of time. The ratio was converted to a temperature by use of the calibration equation (Equation 2). A plot of the surface temperature for the aluminum rod sample at an initial charge voltage of 1.1 kV is shown in Figure 11. At early time, the temperature is small and begins to rise. The maximum steady-state value (T_{ss}) is 300°C and was reached at 10 ms . Data prior to 1 ms contained noise from large dE/dt at the initiation of the discharge and therefore are not considered valid.

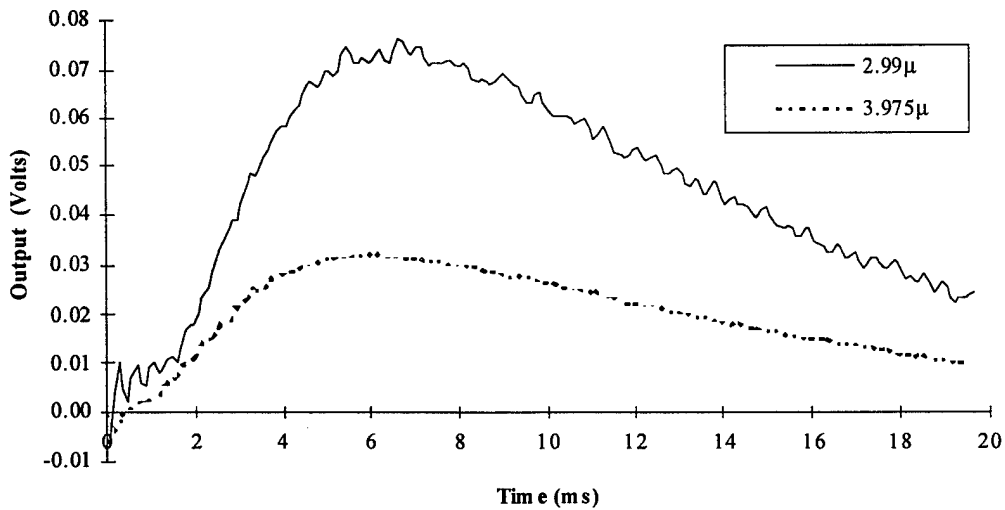


Figure 10. Typical Detector Outputs as a Function of Time for a Pulsed Current.

ii) Steady-State Evaluation of Thermophysical Properties

In order to evaluate the thermophysical properties of the rod samples, it is convenient to fit the measured temperature as a function in time to obtain the maximum steady state temperature (T_{ss}). A function of the form,

$$T(t) = Zt^n, \quad (3)$$

was used to fit the ratio of the infrared data where Z and n are constants for each shot and determined from a regression analysis. A summary of the fitting constants and the time when T_{ss} is reached (t_{ss}) are listed for each shot in Table 1.

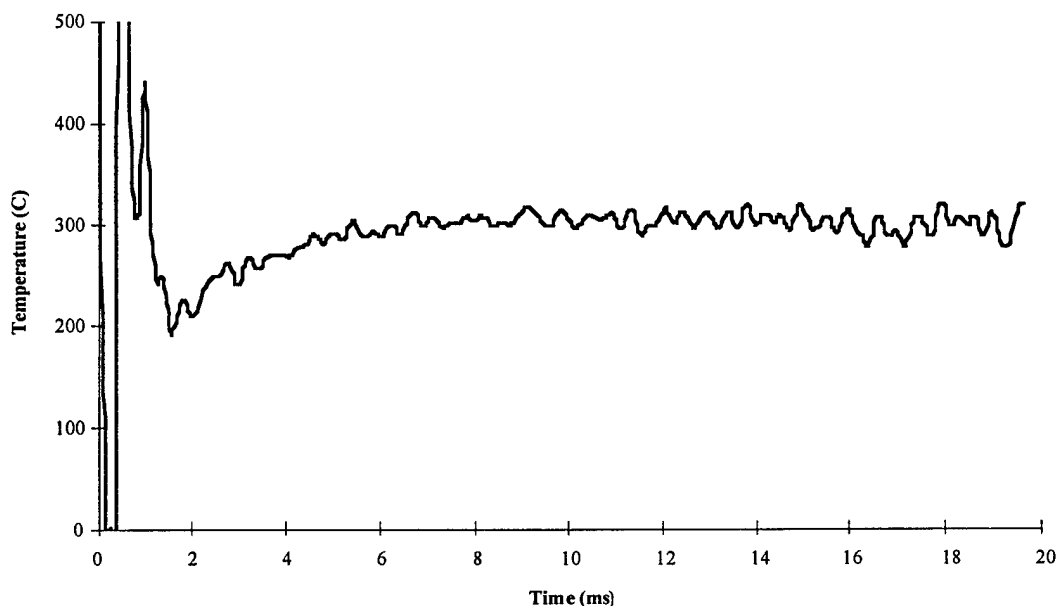


Figure 11. Measured Surface Temperature as a Function of Time ($V_i = 1.1$ kV).

Table 1. Summary of Fitting Constants for Surface Temperature as a Function of Time

Aluminum			
V_i (kV)	n	Z	t_{ss} (ms)
1.0	-0.121	304.1	5
1.1	0.082	245.2	8
1.2	0.173	241.5	12
1.3	0.208	239.3	14
1.4	0.149	294.2	15
1.4	0.143	315.5	18
Copper			
1.4	-0.251	254.8	3
1.6	0.123	183.0	10
1.8	0.133	205.2	12
2.0	0.258	193.2	16

To calculate the specific heat for the rod sample, the fitted value for T_{ss} was used for each shot at the times indicated in Table 1. A value of 25 °C was assumed for the room temperature. The mass of the rod sample (m_r) was calculated from the physical dimensions ($d = 6.35$ mm and $\ell = 101.6$ mm) and aluminum and copper density values of 2,700 kg/m³ and 8,952 kg/m³,

respectively. The energy dissipated in the rod sample was taken at 5 ms. Specific heat, C , was calculated from the approximate expression

$$C = \frac{E}{\Delta T m_r}. \quad (4)$$

The specific heat for both the aluminum and copper rod samples is plotted as a function of T_{ss} in Figure 12. A linear fit to handbook data is also shown in the plot [8]. Extrapolating the data from the experiments to room temperature yields for the specific heat for the aluminum and copper rod samples values of 793 J/Kg/C and 381 J/Kg/C, respectively. These values are within 5% of handbook data at room temperature [8].

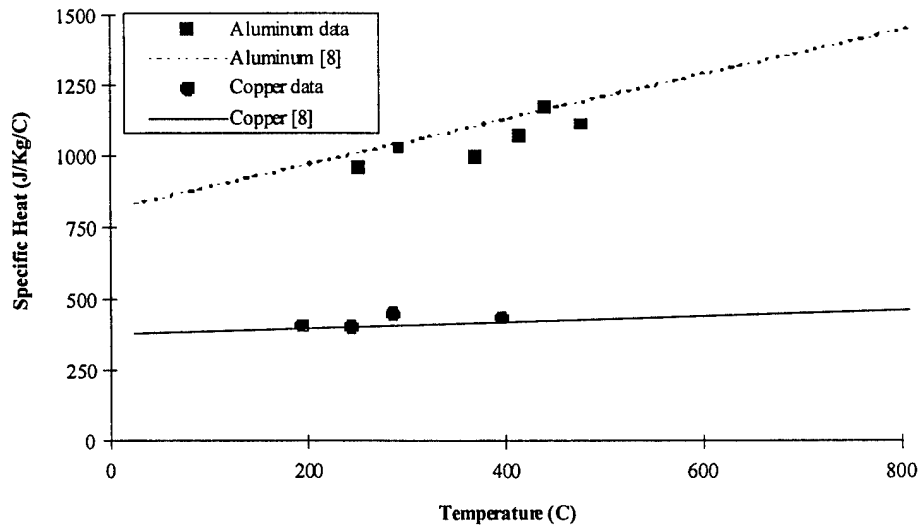


Figure 12. Specific Heat as a Function of Temperature.

The resistance of the rod sample was evaluated as the ratio of V_r/i for times when the current was uniform and had fully diffused through the rod diameter. Uniformity was presumed to occur after the current had reached its maximum value. For this region the inductive contribution toward the measured voltage is negligible. However, as can be seen from the measured data (see Figures 7 and 8), the values for V_r and i are quite small at the time of maximum energy dissipation (5 ms). Therefore, the value for resistivity was calculated from the resistance

and rod sample dimensions at 2.5 ms. The resultant expression is,

$$\rho = \frac{\pi d^2 V_r}{4 i l} \quad (5)$$

The resistivity for both the aluminum and copper rod samples is plotted as a function of T_{ss} in Figure 13. A linear fit to handbook data is also shown in the plot [8, 9]. Extrapolating the data from the experiments to room temperature yields values for the resistivity for the aluminum and copper samples of 42 nΩ-m and 22 nΩ-m, respectively. These values are in agreement with the handbook data at room temperature [8, 9].

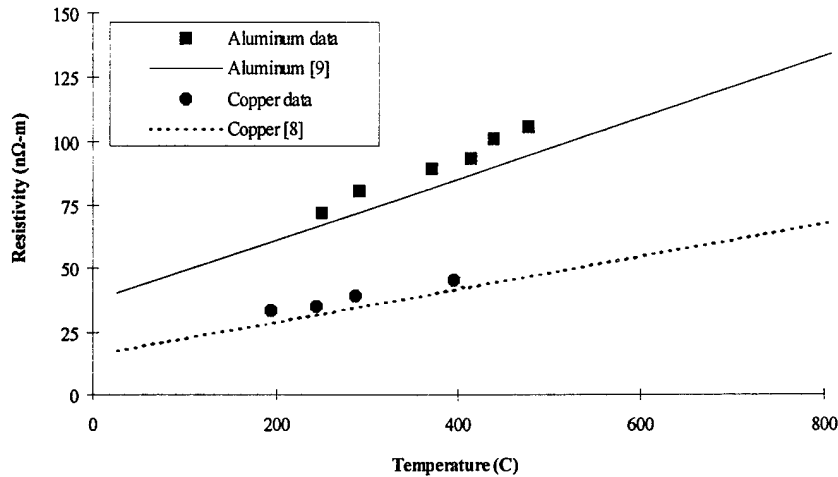


Figure 13. Resistivity as a Function of Temperature.

A parameter of interest to solid armature performance is the specific action [10]. The specific action is related to the temperature rise in a material. This value can be calculated from the thermophysical properties integrated over the temperature range, or can be found from the integral of the square of the current over the pulse duration [11]. The specific action was calculated for each rod sample and is plotted as a function of T_{ss} in Figure 14. Also shown in the figure are data from a prior experiment where the rod sample failed at 1.2 ms during the application of a pulsed, peak current of 165 kA. In this test the specific action was taken at the value just prior to the point at which the voltage became very large (i.e., open circuit). The specific action to cause the aluminum rod to fail was 19,721 A²-s/mm⁴ and corresponds to an

extrapolated measured temperature of nearly 600 °C. This temperature is lower than the melt temperature [12]. Nonetheless, an experimentally determined value for the specific action of 20,000 A²-s/mm⁴ has been found to be an acceptable design limit for solid armatures [10].

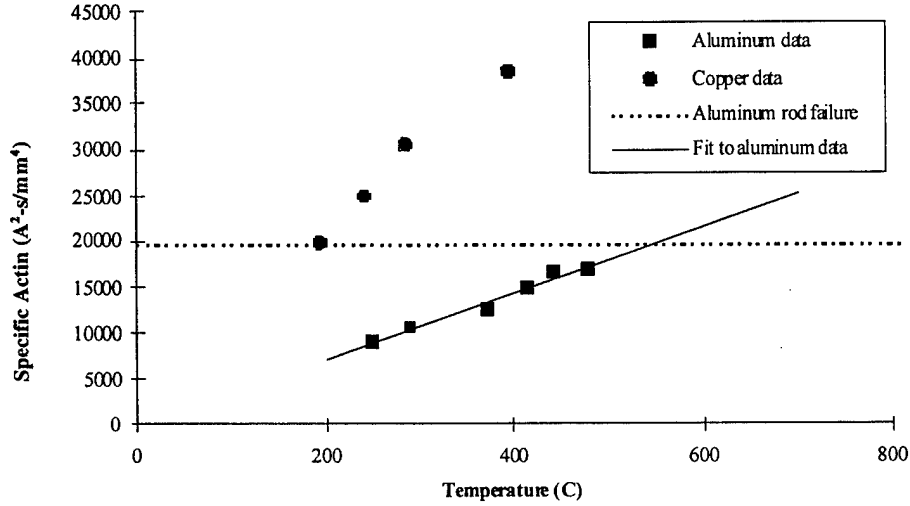


Figure 14. Specific Action as a Function of Temperature.

3. THEORETICAL ASSESSMENT

Calculations were performed in which the magnetic induction and temperature of the rod were obtained as a function of time and space. These calculations were undertaken with a one-dimensional (radial direction) model in which the coupled magnetic and heat-transport equations were solved for conditions appropriate for the experiments. The governing differential equations are

$$\mu\sigma \frac{\partial B}{\partial t} = \frac{\partial^2 B}{\partial r^2} + \frac{1}{r} \frac{\partial B}{\partial r} - \frac{B}{r^2} - \frac{1}{\sigma} \frac{\partial \sigma}{\partial r} \frac{\partial B}{\partial r} - \frac{B}{\sigma r} \frac{\partial \sigma}{\partial r} \quad (6)$$

and

$$\rho \frac{\partial e}{\partial t} = \kappa \frac{\partial^2 T}{\partial r^2} + \frac{\kappa}{r} \frac{\partial T}{\partial r} + \frac{\partial \kappa}{\partial r} \frac{\partial T}{\partial r} + \frac{1}{\mu^2 \sigma} \left(\frac{\partial B}{\partial r} + B/r \right)^2. \quad (7)$$

In these equations σ , ρ , κ , and μ represent the electrical conductivity, the density, the thermal conductivity, and the permeability of the rod, respectively; B , T , and e represent the magnetic induction, the temperature, and internal energy. The temperature is related to the internal energy through the relation

$$e = \int_0^T C dT + H_F \Theta(T - T_m), \quad (8)$$

where H_F is the heat of fusion, C is the specific heat, and Θ is a step function that is equal to zero when T is less than the melt temperature T_m , and is equal to unity when T is greater than T_m . Clearly, melting is assumed to occur at a well-defined temperature T_m .

Equations (6)–(8) are nonlinear and coupled because of the temperature dependence of the various electrical and thermal properties and because of the ohmic heating term (the last term) in Equation (7). The equations must be solved subject to the boundary conditions

$$B(r = 0) = 0$$

$$B(r = r_0) = \frac{\mu i}{2\pi r_0}$$

and

$$\left(\frac{\partial T}{\partial r}\right)_{r=0} = \left(\frac{\partial T}{\partial r}\right)_{r=r_0} = 0, \quad (9)$$

where r_0 denotes the radius of the rod and i denotes the current. The solution of the equations was effected by modifying a computer program employed previously to investigate current and heat transport in solid-armature railguns [1]. Property data employed in the calculations were also taken from [1].

4. CALCULATIONS AND COMPARISON WITH EXPERIMENT

Shown in Table 2 is a summary of both experimental and theoretical results for the ten shots investigated. The temperatures T_{ss} and T_f correspond to the final steady-state temperatures measured in the experiment and predicted by the theory, respectively, whereas T_5 corresponds to the temperature measured at $t = 5 \text{ ms}$. This particular time was of interest because it corresponds very closely to the time at which all the energy had been dissipated in each rod sample. The theoretical values were obtained by numerical calculations with the model described in the preceding section. Each of these temperatures is listed opposite the initial capacitor charge V_i and peak current i_0 for the shot in question.

Table 2. Summary of Surface Temperatures and Pulsed Power Data

Aluminum				
V_i (kV)	i_0 (kA)	T_5 (C)	T_{ss} (C)	T_f (C)
1.0	89.8	230	230	238
1.1	98.7	290	300	284
1.2	109	340	370	345
1.3	116.7	360	410	418
1.4	124.3	370	440	472
1.4	126.1	400	470	475
Copper				
1.4	130.3	180	180	190
1.6	146.5	240	240	240
1.8	163.8	270	290	299
2.0	184.8	310	400	389

It can be seen from the table that there is reasonable agreement between the model predictions T_f and the measured values T_{ss} . Furthermore, the final temperature reached increases with increasing capacitor voltage as should be expected. There does, however, appear to be a significant discrepancy between the values T_5 and T_{ss} . This discrepancy suggests that there was heating of the surface of the rod subsequent to the time at which all the energy had been dissipated. Since it appears unlikely that the surface would be heated by conduction from the interior of an axisymmetric rod, the behavior indicates the possibility of a nonuniform distribution of current on the surface of the rod. A possible source of the maldistribution is the

fixture. It seems reasonable to suspect that the presence of the sample viewport and sample clamp could affect the distribution of the induction field surrounding the rod and, consequently, the current distribution on the rod surface.

Some additional calculations and measurements were undertaken to examine further the possibility of nonuniform current distribution. First, the magnetic induction was measured on the side of the rod opposite the viewport and the result compared with that on the front side. The measurements produced the same values to within about 10%, the experimental accuracy with which the measurements could be made. Consequently, no definite conclusions could be drawn from these measurements. Second, the rod inductance was calculated from the measured voltage and the di/dt data by averaging over the interval 10-25 μs . For the copper rods, the average inductance obtained for the four shots was about 66 nH. This value is in excellent agreement with the high-frequency value predicted from the relation [13]

$$L = 2 \times 10^{-9} \ell (\ln(4\ell/d) - 1). \quad (10)$$

However, for the aluminum rods, the average value obtained was about 54 nH, some 18% smaller than the value for the copper rods. Since the dimensions of the rods, and instrumentation to measure V_r and di/dt were identical, this result supports the contention that the current distribution was not uniform in the aluminum rods. As can be observed from the table, the greatest discrepancy between T_{ss} and T_5 seems to be for the aluminum rods at high capacitor voltages. The accuracy of the temperature-measurement technique is better at higher than lower temperatures. Consequently, the effect is more pronounced at higher initial capacitor voltages.

It is desirable to examine further the impact of a nonuniform current distribution on the rod surface. A rigorous investigation would require the solution of a complicated two-dimensional problem in which symmetry about the rod axis is not assumed. Such a calculation is beyond the scope of this work. However, some estimate of the magnitude of the effect was obtained by adapting as a simple model a rectangular plate for which it was assumed that the current distribution across the width of the plate was nonuniform. The width of the plate was

taken to be equal to the rod diameter, and the thickness was chosen (5 mm) so that the cross-sectional area was the same as that of the rod. The model was assumed to be one-dimensional so all edge effects were ignored. Calculations similar to those described in Section 3, but for a rectangular geometry and a nonuniform current, were then performed.

Typical results of calculations for both the axisymmetric-rod and plate models, as well as the experimental measurements, are shown as a function of time in Figure 15. The calculations performed were for an aluminum rod having a radius r_0 of 3.18 mm. The initial voltage V_i was 1.4 kV and the peak current i_0 was 126.1 kA (see the last entry for aluminum in Table 2). The time-dependent current $i(t)$ used in the calculations was taken from the experimental data and fit to the functional form

$$i = i_0 \sin\left(\frac{\pi t}{2t_1}\right), \quad \text{for } t < t_1$$

and (11)

$$i = i_0 \exp(-(t - t_1)/t_2), \quad \text{for } t > t_1.$$

The time constants t_1 and t_2 were given by the relations: $t_1 = 420 \mu s$, and $t_2 = 1.68 ms$.

For the axisymmetric calculation, the value of the magnetic induction at the surface of the rod was given by Equation (9). The calculated magnetic induction at the surface of the rod is less than 13% of the measurements of B_ϕ scaled to a peak current of 126.1 kA. Diffusion of current into the rod was accounted for. For the plate calculation, the current density was assumed to vary linearly from one value at the front of the plate to another value at the back, with the constraint that the total current is given by Equation (11) at any time. Thus, diffusion was neglected in these calculations. However, since the time scale for diffusion is considerably smaller than the time scale of the current pulse, this approximation was not felt to be particularly restrictive.

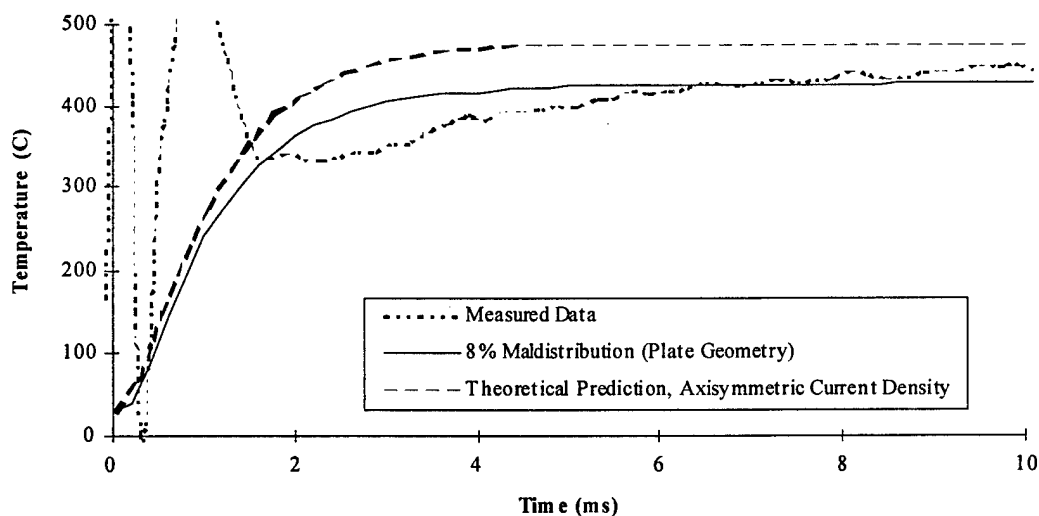


Figure 15. Measured and Predicted Surface Temperature ($V_i = 1.4 \text{ kV}$).

As can be seen in the figure and as should be expected, the axisymmetric model (dashed curve) predicts that the final steady-state temperature T_f (about 475°C) was reached at about 5 ms , or at the time at which the dissipated energy reached its final value. The measured temperature (dotted curve) appears to be approaching this final value also, but only after times considerably longer than 5 ms . The calculation performed for the plate geometry (solid curve) was based on the assumption that the current density at the front of the plate (viewport) was 8% smaller than that at the back, and that the linear variation described earlier was obeyed. The value of 8% was somewhat arbitrarily chosen, but constrained to be within the 10% experimental-error bounds described earlier. As can be seen, the temperature predicted by this model is more nearly in agreement with the measured value than is the temperature predicted by the axisymmetric model. The slow rise in temperature at times later than 5 ms can be attributed to conduction from the back to the front of the plate. Although the analysis is clearly limited, the results do seem to suggest that a fairly small maldistribution in current can account for the discrepancy between the theoretical and experimental results.

It is also interesting to note that calculations carried out with the symmetric model for a peak current of 165 kA predicted a maximum temperature at the rod surface of 527°C , i.e., well below the melt temperature. However, the plate model, again with the 8% difference in current

density, predicted that the back of the plate reached the melt temperature at about 1.4 ms . It was also at about this time that the rod was observed to fail in experiments conducted at this current. This observation seems to lend some additional credence to the assumption of a nonuniform current on the rod surface.

In addition to the temperatures, a comparison was also made of the voltage measured experimentally with that obtained with the axisymmetric model. The resistive component of the voltage was calculated by computing the total power dissipated resistively as a function of time in the rod, and dividing the result by the total current. The measured voltage generally includes both inductive and resistive components and it is necessary to subtract the inductive contribution prior to undertaking the comparison. That contribution was computed from the measured di/dt data and the assumed inductance of 54 nH for the aluminum rod. Changes in the rod inductance with time were not accounted for. A plot of the theoretical and measured resistive voltages is shown in Figure 16. It can be seen that there is relatively good agreement between the data and calculated results; the largest discrepancy is at peak current and is less than 15% . A small maldistribution in the current distribution appears to be sufficient to account for the discrepancy.

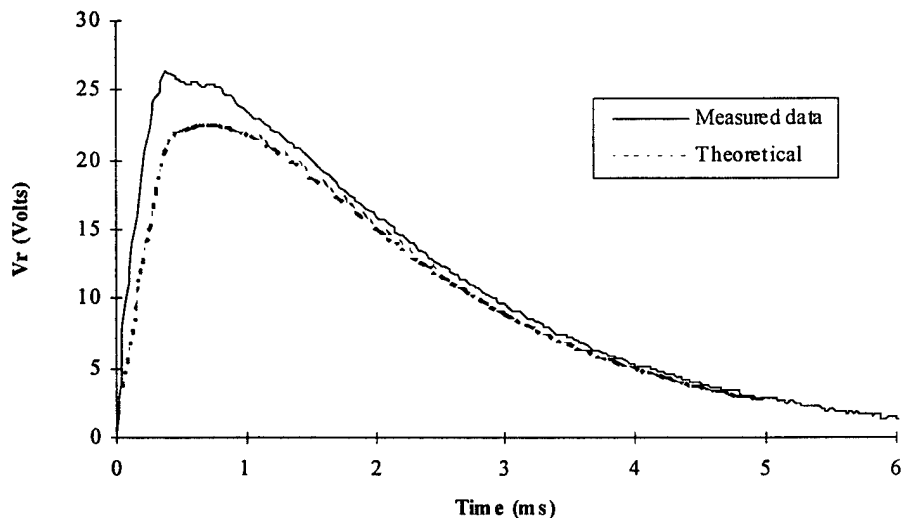


Figure 16. Resistive Voltage Contribution Across the Rod Sample.

5. IMPLEMENTATION IN A MOVING ARMATURE

Implementation of the thermal measurement technique for a moving solid armature is somewhat more difficult than the static measurements on the rod sample. The emitted energy would have to be transmitted extremely close from the armature surface. This application necessitates the use of a fiber optic cable to transmit the energy from the armature surface to the detector windows. A glass-clad, fluoride-glass, multistranded fiber optic bundle will meet this need. Ideally, a custom fiber optic cable would be constructed from a combination of glass-clad fluoride-glass fibers and polymer-clad chalcogenide glass fibers. By using the combination of these two types, wavelengths from 1 to $7\text{ }\mu\text{m}$ could be transmitted with tolerable optical losses. A cable length of approximately 1.5 m should allow the detectors to be placed sufficiently far from the PPS and gun structure to minimize the effects of stray electromagnetic radiation which could contaminate the output of the detector and amplifiers. The placement of the detectors would be close enough to the experiment to reduce transmission losses. The bundle should be evenly divided into two smaller bundles forming a 0.45 m long bifurcation. The bifurcation allows the two detectors to view the source simultaneously. One end of the cable should be terminated into a bundle supported by a metal ferule. This metal ferule would facilitate holding a lens. At the single source end the lens, which would make the source rays parallel entering the bundle, would collimate the infrared emission from the armature. At each of the bifurcated ends, the lens would focus the emissions onto the active area of the detector. The optics and support structure could be cooled to help reduce thermal noise. The fiber optic cable, although flexible, should be mechanically supported along its length since it has been shown that the shock from arcing can fracture an unsupported cable. Additionally, the straightness of the cable has also been shown to affect the optical attenuation.

The custom fiber optic cable can transmit the wide band of wavelengths, which is necessary for an accurate temperature determination. The filtering within the transmitted band also plays an important role in accurately determining the temperature. Filters having a narrow bandwidth of approximately $0.1\text{ }\mu\text{m}$ and centers of $2.99\text{ }\mu\text{m}$ and $5.20\text{ }\mu\text{m}$ would be adequate selections for determining the temperatures from less than $200\text{ }^{\circ}\text{C}$ to greater than $700\text{ }^{\circ}\text{C}$.

Because of the time scale of the temperature measurement, the frequency response of the detectors and their amplifiers affects the resolution. The measurement of the moving armature requires that the frequency response be such that it can track the change in temperature as the armature passes by the fiber optic cable. Capturing a *1-mm* round profile of an armature traveling at *60 m/s* requires that the bandwidth be at least *120 kHz*. The amplifier and detector pairs used in the measurement of the surface temperature of the rod sample meet this specification. To help reduce electrical noise generated during the pulse discharge, the amplifier and detector pair should be enclosed in a shielded enclosure.

High amplifier gain is necessary because of the small area of observed emissions, attenuation in the fiber optic cable and optics, and the less than ideal quantum efficiency of the detectors. Due to the steep rise in emissive energy prior to peak, the gain of the amplifier must be sufficient to yield a usable signal in the lower amplitudes of the "prior to peak" region. This high gain also makes dynamic range an important factor because, as can be seen from Figure 2, the peak emissive output changes by approximately two orders of magnitude from *200 °C* to *700 °C*.

In order to generate the isothermal data with a single, bifurcated fiber optic cable and dual detector amplifier pairs, the cable must be capable of observing a *1-mm* diameter at the surface of the armature. The position of the armature as it accelerates must be determined relative to the location of the fiber optic cable. An optical position detector could be constructed to meet this requirement. By performing multiple identical shots, overlapping thermal data can be generated. Combining these axial strips will then create a thermal profile for the armature surface. For a *15-mm* square bore railgun, eight separate firings with identical conditions must be assimilated in order to achieve an isothermal plot of the armature half-surface. Because this technique requires multiple shots, it is imperative that the position and performance of the armature be known precisely during the time they are being observed by the detectors.

6. SUMMARY AND CONCLUSIONS

A technique was developed to measure the surface temperature of an electrically pulsed material. The time resolution of the technique is sufficient to reveal a nonuniform distribution in the current density in the rod sample. Use of this technique extends the time resolution achieved with thermocouples by an order of magnitude. The technique could be refined further by using a fiber optic cable and minimal shielding. Additionally, thermophysical properties for the rod samples were determined from the measured steady-state temperatures and are consistent with handbook values.

A model based on a one-dimensional consideration of coupled Maxwell and heat transport equations was developed. The predicted thermal results were in good agreement with the measured data. However, some discrepancies exist with respect to the time evolution of the temperature. A slightly nonuniform distribution in current, consistent with the measurement of the azimuthal component of the magnetic induction of the rod and the rod inductance, is sufficient to account for an increased thermal load on the side opposite the sample viewport. Consequently, the maximum measured surface temperature occurs after maximum energy is dissipated in the rod sample. Furthermore, the increased temperature due to an 8% increase in the current at 165 kA is sufficient to melt the rear of the rod surface while the front surface is below the melt temperature. This result is consistent with the observed electrical data and lower than expected specific action to cause failure in the rod sample.

During the course of this investigation numerous issues with regard to the hardware and its implementation were uncovered. While most of the issues were resolved, much work needs to be done to reliably measure the temperature distribution in a moving solid armature without placing the hardware at risk. In particular, care must be taken with the detector and fiber optic cable, as these components are essential and costly.

ACKNOWLEDGEMENTS

This work was supported by the continuous efforts of the Institute for Advanced Technology (IAT) staff. Specifically, the authors are especially grateful to Mr. Patrick Sullivan for his generosity and patience. Significant technical review and helpful comments were provided by Dr. V. Thiagarajan. Dr. J. Parker, IAT, provided very useful discussions on the non-uniform distribution of current. The authors also wish to thank Mr. Kenneth Paxton, DSI, for experimental support and Mr. Calvin Le, ARL, for calibration of the voltage probe and magnetic induction sensors. The authors acknowledge the assistance of Dr. R. Beyer, Dr. R. Pesce-Rodriguez, and Dr. G. Thompson, ARL, for providing equipment to support the experiments. This work was also supported by the U.S. Army Research Laboratory (ARL) under contract DAAA21-93-C-0101.

REFERENCES

- [1] Powell, J. and Zielinski, A. E., "A Preliminary Study of Wear in the Solid-Armature Railgun," Institute for Advanced Technology Technical Report, IAT.R 0156, December 1997.
- [2] Hsieh, K., "A Lagrangian Formulation for Mechanically and Thermally Coupled Electromagnetic Diffusive Processes with Moving Conductors," *IEEE Transactions on Magnetics*, Vol. 31, No. 1, pp. 604-609, January 1995.
- [3] Jamison, K., Petresky, H., Beavers, F., Eggers, P., Guinto, S., Holland, M., and Vrable, D., "Thermal Loading and Heat Removal from a Sequentially Fired Railgun," *IEEE Transactions on Magnetics*, Vol. 31, No. 1, pp 314-319, January 1995.
- [4] Micali, J., Derbridge, T., Heydt, R., and Blanchard, K., "Railgun Bore Heat Transfer Gage," WL/MN-TR-91-67, Astron Research and Engineering Final Report, Eglin AFB, April 1992.
- [5] *Modern Physics*, Kenneth Krane, John Wiley & Sons, Inc., New York, 1983, p. 65.
- [6] Jamison, K. A., Stearns, R. E., Klug, R. B., and Ford, R. D., "High Energy Cable Development for Pulsed Power Applications," *IEEE Transactions on Magnetics*, Vol. 27, No. 1, pp. 374-379, January 1991.
- [7] *VuPoint 3 Users Guide*. S-Cubed, A Division of Maxwell Laboratories, Inc., P.O. Box 1620, La Jolla, CA, 92038.
- [8] *Thermophysical Properties of High Temperature Solid Materials*, Volume 1: Elements, Thermophysical Properties Research Center, Purdue University, Y. S. Touloukian (Editor).
- [9] Olafsson, P., Sandstrom, R., and Karlsson, A., "Comparison of Experimental, Calculated, and Observed Values for Electrical and Thermal Conductivity of Aluminum Alloys," *Journal of Materials Science*, 32, 1997, pp. 4383-4390.
- [10] Price, J. H. and Yun, H. D., "Design and Testing of Integrated Metal Armature Sabots for Launch of Armor Penetrating Projectiles from Electric Guns," *IEEE Transactions on Magnetics*, Vol. 31, No. 1, pp. 219-224, January 1995.
- [11] Tucker, T. J. and Toth, R. P., "EBW1: A Computer Code for the Prediction of the Behavior of Electrical Circuits Containing Exploding Wire Elements," Sandia Laboratories Technical Report, SAND-75-0041, April 1975.
- [12] Marshall, R. A., "Current Carrying Capacity of Solid Armatures for Railguns at Zero Speed," *IEEE Transactions on Magnetics*, Vol. 33, No. 1, pp. 125-128, January 1997.
- [13] Grover, F. E., *Inductance Calculations*, Van Nostrand: New York, 1946.

APPENDIX

C Program to calculate the energy output and ratio from 2 thermal sources.

Implicit Real (H,I,K,L,M)

C Inputs

C Emmisivity

Emm=0.47

C Temperature (Source)

Tmin=50.0

Tmax=1000.0

Dt=50.0

C Minimum wavelength

Lmin=1.0e-6

C Maximum wavelength

Lmax=6.0e-6

C Integration step

Dl=1.0e-9

C First filter characteristics

C A1, Transmittance, attenuation factor at the center frequency

A1=0.74

C Center frequency

Cen1=2.99e-6

C Half-power bandwidth

$\text{Sig1}=0.098$

C Fudge factor filter characteristics

$F1=0.3575$

C Amplifier gain

$\text{yg1} = 1.0\text{e}6$

C Second filter characteristics

C A2, Transmittance, attenuation factor at the center frequency

$A2=0.74$

C Center frequency

$\text{Cen2}=5.2\text{e-}6$

C Half-power bandwidth

$\text{Sig2}=0.111$

C Fudge factor filter characteristics

$F2=1.422$

C Amplifier gain

$\text{yg2} = 1.0\text{e}5$

C Constants

C Plank

$h=6.626\text{E-}34$

C Boltzman

$$k=1.38e-23$$

C Speed of Light

$$c=2.99e8$$

C Conversion to Kelvin

$$T_0=273.15$$

$$FCT=1.e6$$

$$c1=2.0*pi*H*(C**2.0)$$

$$c2=(H*C)/K$$

Do 500 T= Tmin, Tmax, Dt

$$T_{mp}=T+T_0$$

$$E1=0.0$$

$$E2=0.0$$

$$r=0.0$$

DO 200 L = Lmin, Lmax, D1

$$TRC1=A1*\exp(-((FCT*(L-Cen1))**2.0)/(F1*Sig1**2.0))$$

$$TRC2=A2*\exp(-((FCT*(L-Cen2))**2.0)/(F2*Sig2**2.0))$$

$$Temp1=(C1/(L**5.0))$$

$$Temp2=(1.0/((\exp((C2/(T_{mp}*L))))-1.0))$$

$$Ex1 = xg1 * Emm*Temp1*Temp2$$

$$Ex2 = xg2 * Emm*Temp1*Temp2$$

$$E1=E1 + (Ex1*TRC1) * D1$$

$$E2=E2 + (Ex2*TRC2) * D1$$

200 Continue

If(E2 .ne. 0.0) Then

$r = E1/E2$

Else

End IF

Write(25,900)T, r, E1/1.0e6, E2/1.0e6

900 Format(1x,F7.1,1x,F14.5,1x,F14.5,1x,F14.5)

500 Continue

Stop

End

Distribution List

Administrator
Defense Technical Information Center
Attn: DTIC-DDA
8725 John J. Kingman Road,
Ste 0944
Ft. Belvoir, VA 22060-6218

Director
U.S. Army Research Lab
ATTN: AMSRL OP SD TA
2800 Powder Mill Road
Adelphi, MD 20783-1145

Director
U.S. Army Research Lab
ATTN: AMSRL OP SD TL
2800 Powder Mill Road
Adelphi, MD 20783-1145

Director
U.S. Army Research Lab
ATTN: AMSRL OP SD TP
2800 Powder Mill Road
Adelphi, MD 20783-1145

Army Research Laboratory
AMSRL-CI-LP
Technical Library 305
Aberdeen Prvg Grd, MD 21005-5066

Dr. John P. Barber
IAP Research, Incorporated
2763 Culver Avenue
Dayton, OH 45429-3723

Dr. J. Batteh
SAIC
1225 Johnson Ferry Rd
Suite 100
Marietta GA 30068

Mr. Dave Bauer
IAP Research, Incorporated
2763 Culver Avenue
Dayton, OH 45429-3723

J. Bennett
U.S. Army TACOM-ARDEC
FSAE-GCSS-TMA/Bldg. 354
Picatinny Arsenal, NJ 07806-5000

M. Bourham
North Carolina State University
Dept. of Nuclear Eng.
Box 7909
Raleigh, NC 27695-7909

Dr. William D'Amico
U.S. Army Research Laboratory
Attn: AMSRL-WM-B
Aberdeen Prvg Grd, MD 21005-5066

Dr. Mircea Driga
University of Texas at Austin
Dept. of Electrical & Computer Eng.
Mail Code 60803
Austin, TX 78712

Dr. Brad Forch
U.S. Army Research Laboratory
AMSRL-WM-B
Aberdeen Prvg Grd, MD 21005-5066

C. Gilman
Maxwell Physics International
2700 Merced Street
P.O. Box 5010
San Leandro, CA 94577-0599

Dr. Clinton Hollandsworth
U.S. Army Research Laboratory
AMSRL-WM-WD
Aberdeen Prvg Grd, MD 21005-5066

Mr. Albert Horst
Chief, Propulsion and Flight Division
Army Research Laboratory
ATTN: AMSRL -WM-B
Army Research Laboratory
Aberdeen Prvg Grd, MD 21005-5066

Dr. William Isbell
ATA Associates
P. O. Box 6570
Santa Barbara, CA 93160-6570

Dr. Keith A. Jamison
Science Applications International Corp.
1247-B N. Eglin Parkway
P. O. Box 126
Shalimar, FL 32579

R. Johnson
UDLP
MS M170
4800 East River Rd
Minneapolis, MN 55421-1498

J. Kezerian
Maxwell Technologies
9244 Balboa Avenue
San Diego, CA 92123

Mr. David Lyon
U.S. Army Research Laboratory
AMSRL-WM-BC
Aberdeen Prvg Gnd, MD 21005-5066

Distribution List

Dr. Ingo W. May
Office of the Director
U.S. Army Research Laboratory
ATTN: AMSRL -WM
Bldg#4600
Aberdeen Prvg Grd, MD 21005-5069

Mr. Robert J. Taylor
Lockheed Martin Vought Systems
M/S: WT-21
P.O. Box 650003
Dallas, TX 75265-0003

Dr. Peter Plostins
U.S. Army Research Lab
AMSRL-WM-BC
Aberdeen Prvg Grd, MD 21005-5066

Mr. Alan Walls
Center for Electromechanics
The University of Texas at Austin
PRC, Mail Code R7000
Austin, TX 78712

Dr. John Powell
U.S. Army Research Laboratory
Attn: AMSRL-WM-WD
Aberdeen Prvg Grd, MD 21005-5066

Tim Wolfe
Maxwell Laboratories, Inc.
9244 Balboa Avenue
San Diego, CA 92123

Dr. S. Pratap
Center for Electromechanics
The University of Texas at Austin
BRC, EME 133
10100 Burnet Road
Austin, TX 78758-4497

Dr. Gloria P. Wren
Mathematician
U.S. Army Research Lab
Attn: AMSRL-WM-B
Aberdeen Prvg Grd, MD 21005-5066

J. Reidy
Maxwell Technologies
9244 Balboa Avenue
San Diego, CA 92123

Mr. Alex Zielinski
U.S. Army Research Laboratory
AMSRL-WM-BC
Aberdeen Prvg Grd, MD 21005-5066

Dr. Jim Sarjeant
State University of New York at Buffalo
312 Bonner-Elect. Engr.
University at Buffalo - SUNY/AB
P. O. Box 601900
Buffalo, NY 14260-1900

Dr. Edward M. Schmidt
U.S. Army Research Laboratory
Attn: AMSRL-WM-B
Aberdeen Prvg Grd, MD 21005-5066